Arrangement of Maghemite Nanoparticles via Wet Chemical Self-Assembly in PS-b-PNIPAM Diblock Copolymer Films

Yuan Yao,[†] Ezzeldin Metwalli,[†] Bo Su,[†] Volker Körstgens,[†] Daniel Moseguí González,[†] Anna Miasnikova,[‡] Andre Laschewsky,[‡,§] Matthias Opel,[∥] Gonzalo Santoro,[⊥,#] Stephan V. Roth,[⊥] and Peter Müller-Buschbaum*,[†]

[†]Technische Universität München, Physik-Department, Lehrstuhl für Funktionelle Materialien, James-Franck-Str. 1, 85748 Garching, Germany

[‡]Institut für Chemie, Universität Potsdam, Karl-Liebknecht-Str. 24-25, 14476 Potsdam-Golm, Germany

[§]Fraunhofer Institut für Angewandte Polymerforschung IAP, Geiselbergstrasse 69, 14476 Potsdam-Golm, Germany

[∥]Walther-Meissner-Institut, Bayerische Akademie der Wissenschaften, Walther-Meissner-Strasse 8, 85748 Garching, Germany

[⊥]Deutsches Elektronen-Synchrotron DESY, Notkestrasse 85, 22603 Hamburg, Germany

[#]Instituto de Ciencia de Materiales de Madrid, ICMM-CSIC, sor Juana Inés de la Cruz 3, Cantoblanco, 28049 Madrid, Spain

⑤ *Supporting Information*

ABSTRACT: The structure and magnetic behavior of hybrid films composed of maghemite (γ-Fe_2O_3) nanoparticles (NPs) and an asymmetric diblock copolymer (DBC) polystyrene$_{61}$-*block*-poly$N$-isopropylacrylamide$_{115}$ are investigated. The NPs are coated with PS chains, which allow for a selective incorporation inside the PS domains at different NP concentrations. Upon incorporation of low amounts of NPs into the DBC thin films, the initial parallel (to film surface) cylinder morphology changes to a well ordered, perpendicularly oriented one. The characteristic domain distance of the DBC is increased due to the swelling of the PS domains with NPs. At higher NP concentrations, the excess NPs which can no longer be embedded in the PS domains, are accumulated at the film surface, and NP aggregates form. Irrespective of NP concentration, a superparamagnetic behavior of the metal oxide-DBC hybrid films is found. Such superparamagnetic properties make the established hybrid films interesting for high density magnetic storage media and thermoresponsive magnetic sensors.

KEYWORDS: *nanocomposites, maghemite nanoparticles, block copolymer, GISAXS, hybrid films*
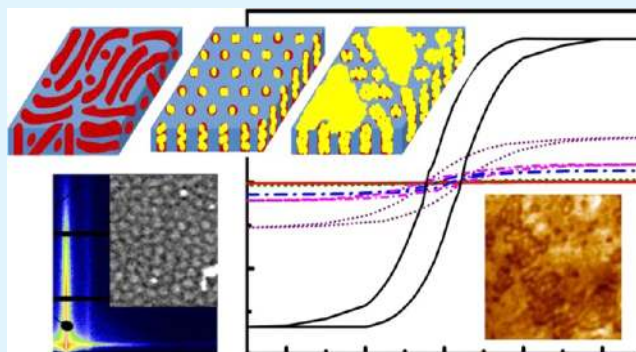
1. INTRODUCTION

Nanostructured hybrid composites consisting of an insulating polymer template with embedded inorganic, functional nanoparticles (NPs) attract great attention as novel advanced materials due to their interesting physical properties.[1−5] Targeting substantial advantageous electrical, mechanical, optical, magnetic, and thermal properties, which are endowed by adding versatile kinds of functional NPs, has successfully rendered many applications of band gap materials, wrappings, sensors, magnetic storage media, spin-dependent electron transport devices, diagnostic medical functions, catalysis, and thermo-responsible materials.[6−13] In comparison to bulk materials, NPs have been proven to significantly enhance the desired performance due to the large surface-to-volume ratio. For the particular purpose of magnetic applications, such as data storage devices and magnetic sensors, maghemite (γ-Fe_2O_3) NPs are favorable because of their lower magnetic remanence and coercivity as compared with bulk magnetic materials.

The realization of desired properties is largely dependent on the arrangement of the NPs and can be tuned by using host matrixes.[14−16] Nanoscale periodic ordered templates can be formed via self-assembly making use of the microphase separation of diblock copolymers (DBCs), which are composed of two chemically incompatible blocks linked by a covalent bond. By selecting different chemical blocks, changing their molecular weights, and tuning the polymer block ratio, versatile morphologies of spheres, cylinders, gyroids, and lamella can be fabricated with a characteristic length scale ranging from about 10 to 100 nm.[3,17,18] In the case of DBC thin films, in addition to the shape and size of the microphase separation

morphologies, the orientation with respect to the film surface—which can be parallel, perpendicular, or randomly arranged—is crucial for the applications as well. Therefore, producing an appropriately oriented, highly periodic, ordered DBC matrix is of high interest for fabricating well-defined NPs-DBC hybrid nanocomposites.[19,20] On the basis of several different approaches, such as vapor deposition, plasma deposition, electrophoresis, dip-coating, and wet coating, the arrangement of the NPs inside the DBC matrix can be controlled.[2] Particularly interesting are wet chemical approaches, which use ink-type mixtures of NPs and DBC, because such approaches would allow for large scale fabrication methods such as printing or spray coating.[21] A prerequisite for such an approach is the use of functionalized NPs to promote a preferential affinity to one of the DBC blocks.[22] Properly functionalized NPs exhibit an enthalpic driving force for the selective deposition of the NPs inside one domain of the microphase separated structure during the self-assembly process of the NPs/DBC mixture.[23,24] Moreover, such proper coating of the NPs can prohibit self-aggregation of the NPs in the polymer phase to some extent.[25] Upon incorporation of NPs in the DBC matrix, the original DBC morphology can be modified and deviate from that of the pure DBC due a change of the free energy density. As a consequence, different morphologies can be achieved by combining a DBC template together with NPs.[26] In this sense, several related investigations have been reported in literature. Zhang et al. reported that poly(ethylene oxide) (PEO)-functionalized CdSe nanorods were successfully assembled into the channels and pores provided by polystyrene-*block*-poly(methyl methacrylate) (PS-*b*-PMMA) DBC templates, due to the PEO-functional surface ligand coverage of the nanorods, whereas the other alkane-covered CdSe nanorods are not compatible with this assembly process.[27] Lo et al. systematically investigated several aspects of the effects on the morphology of self-assembled polystyrene-*block*-poly 2-vinylpyridine (PS-*b*-PVP) DBC/surface modified NPs hybrid nanocomposites, including nanorods length, NP size, NP concentration and molecular properties of DBC.[25,28,29] For a similar hybrid system with magnetic pyridine-grafted Fe₂P nanorods, at short rod lengths, nanorods are selectively sequestered into PVP domains due to preferential interaction between pyridine-tethered nanorods and PVP, and they align parallel to the interfaces between PS and PVP domains. However, extensive rod aggregation and macrophase separation happen with long lengths and high nanorod concentration.[28] Additionally, the thiol-terminated polystyrene-stabilized Pd NP distribution was found to strongly depend on the relative size between the NP diameter, d, and the PS domain periodic distance, D. At $d/D \approx 0.3$, NPs self-assembly is favored in the PS domains and cause order−order transitions of the nanocomposite. At intermediate d/D, NP aggregations were observed and disorder morphologies of DBC are induced; whereas, at $d \sim D$, NP-aggregates were observed even at low NP concentration.[29]

In previous studies, we have investigated the evolution of nanostructures in NPs/DBC hybrid nanocomposites consisting of various types of DBCs and metal-oxide NPs having different surface modifications.[30−36] These investigations used DBC such as polystyrene-*b*-poly(methyl methacrylate), which consist of two rather hydrophobic blocks. In the present investigation we extend this approach to a different class of DBC. We select the asymmetric DBC polystyrene₆₁-*block*-polyN-isopropylacrylamide₁₁₅, which is composed of a hydrophobic PS block and a hydrophilic PNIPAM block. The polymer PNIPAM is among the most explored thermoresponsive polymers.[37−39] However, the majority of the studies related to PNIPAM have focused on wet swollen films, the water induced swelling and thermoresponsive behavior or were carried out in aqueous solutions. Only very few studies explored dry PNIPAM films.[40−42] To our knowledge, so far no investigation has focused on the arrangement of magnetic NPs inside a PNIPAM related host DBC film. The goal of the present investigation is to explore the morphological evolution of metal oxide DBC hybrid films, fabricated with structure-directing PS-*b*-PNIPAM DBC template upon incorporation of different concentrations of PS-coated γ-Fe₂O₃. On the basis of the understanding of the morphology of γ-Fe₂O₃/PS-*b*-PNIPAM films further studies can address the humidity-dependent swelling, thermo-responsible switching, and humidity-dependent magnetic properties of the metal-oxide DBC hybrid nanocomposite films. Moreover, based on the methodology of selective γ-Fe₂O₃ NPs incorporation in block copolymer scaffolds and subsequent polymer degradation, a magnetic nanodots array can be created. Such a type of array with perpendicularly aligned magnetic nanodots is considered to be developed for future storage devices due to the fact that its potential storage may reach over 100 times more than the current hard drives.[43−46] To enable data storage application, the magnetic nanoparticles should be larger than a critical size to combat the superparamagnetic limit (fluctuation of magnetization due to thermal agitation). These nanodots can be considered as a great number of tiny magnets capable of switching polarity to represent binary digits.[43−46] Hence, the nanodots-based storage system can provide much higher storage density. In general, the target applications will be switchable high density magnetic storage media and thermoresponsive magnetic sensors. All films have been fabricated identically with spin-coating at room temperature at ambient conditions without any further post-treatment steps. The systematic evolution of nanostructures of the film surface is characterized with scanning electron microscopy (SEM). Additional information about the film topography such as root-mean-square (rms) roughness values are determined by atomic force microscopy (AFM). In addition, the inner film morphology is probed with the nondestructive reciprocal space technique grazing incidence small-angle X-ray scattering (GISAXS), which delivers structural characteristics with a high statistical significance, whereas film thicknesses are examined with surface profilometry. Finally, the application relevant magnetic behavior is probed with a magnetic property measurement system (MPMS) of a superconducting quantum interference device (SQUID) as a function of NP concentration and temperature.

2. EXPERIMENTAL SECTION

2.1. Materials. The investigated asymmetric diblock copolymer polystyrene₆₁-*block*-polyN-isopropylacrylamide₁₁₅, denoted PS-*b*-PNIPAM, was synthesized via consecutive RAFT polymerizations of styrene and NIPAM using *n*-S-butyl-S′-benzyltrithiocarbonate as chain transfer agent. Details of the synthesis protocols and polymer characterizations for such types of diblock copolymer are described elsewhere.[47,48] The number-average molar mass and weight fraction of the PS block were 6.7 kg/mol and 0.32, respectively, while the polydispersity of the DBC was 1.14. Thus, a cylinder morphology was expected for bulk PS-*b*-PNIPAM samples.[17] The surface of the used maghemite nanoparticles (γ-Fe₂O₃) was modified by fully coating with PS chains, synthesized from α-lithium polystyrenesulfonate (LPSS, obtained from Heidelberg University, Heidelberg, Germany) with a

molar mass of 7.5 kg/mol. The synthesis procedures are presented in details elsewhere.[36,49] The diameter of the NP was 6.5 nm with a log-normal size distribution (width 20%). Details about the characterization of the NPs, including the size and the chemical composition, with small-angle X-ray scattering (SAXS) and Mössbauer spectroscopy techniques, can be found elsewhere.[33] The 1,4-dioxane, dichloromethane, ammonia solution, and hydrogen peroxide were supplied by Carl Roth GmbH. Silicon wafers (Si 100, n-type) were purchased from Silchem (Richmond Hill, Ontario, Canada).

2.2. Sample Preparation. Silicon wafers with a native oxide layer on the surface were used as solid substrates for the hybrid films. In the applied basic cleaning protocol,[40,50] the Si substrates were immersed in dichloromethane (purity ≥99.5%) at 46 °C for 30 min, followed by copious rinsing with deionized water. Then, to remove any organic traces, Si substrates were placed into a basic bath (30 mL NH_3, 30%; 30 mL H_2O_2, 30%; 350 mL deionized water) at 76 °C for 2 h. Afterwards, Si substrates were stored shortly in deionized water. Before spin-coating, all possible traces from the basic bath were removed by repeatedly rinsing the Si substrates with deionized water, followed by thorough N_2 blow drying. Due to the used cleaning procedure, a hydrophilic silicon oxide layer of 1 nm was established at the Si surface.[40]

NPs/DBC solutions were prepared by using 1,4-dioxane (purity ≥99.5%) as a solvent. On the basis of previous investigations, 1,4-dioxane is an appropriate solvent for obtaining smooth and homogeneous films in combination with the used basic substrate cleaning.[40,41] To reach the desired film thickness, a fixed polymer concentration of 45 mg/mL was used. The weight ratio of γ-Fe_2O_3 NPs with respect to the DBC PS-b-PNIPAM was varied (0, 0.1, 0.5, 1, 3, 7, and 15 wt %) in the present investigation. Using an identical preparation procedure, all investigated metal oxide NPs/DBC hybrid films were prepared by spin-coating (acceleration time 9 s, spinning speed 2000 rpm, and spin-coating time 30 s) at ambient conditions (room temperature 22 °C and relative humidity 40%). No further postproduction treatment of the as-prepared films was employed.

2.3. Characterization Techniques. *2.3.1. Profilometry.* Film thicknesses were measured with a surface profilometer (Dektak XT Surface Profiler, Bruker) after lifting off part of the film from the substrate with the help of a plastic knife. The profilometry measurements were performed at a slow scan speed of 1 μm/s and a stylus force of 9.8 μN.

2.3.2. Scanning Electron Microscopy (SEM). SEM measurements were performed with an NVision40 FESEM by Carl Zeiss AG with an accelerating voltage of 2 kV and a working distance of 1.2 mm. The software Gwyddion 2.37 was used for further image processing and analyzing.[51] To check the sample homogeneity, the SEM micrographs were taken at several selected spots, which were located close to the four corners and at the center of each sample.

2.3.3. Atomic Force Microscopy (AFM). For 3D mapping of the film surface, AFM measurements were performed with a JSPM-5200 AFM (JEOL U.S.A., Inc.) using a noncontact mode in ambient conditions at room temperature. The mounted cantilevers (ULTRA-SHARP NSC35/ALBS, MikroMasch) had tips with a curvature radius of 15 nm, with a force constant of 7.5 N/m and with a resonance frequency of 165 kHz. The obtained AFM data were further processed and analyzed by the software WinSPM v2.14.

2.3.4. Grazing Incidence Small-Angle X-ray Scattering (GISAXS). The GISAXS measurements were performed at the beamline P03 Micro- and Nanofocus X-ray Scattering (MiNaXS) of the PETRA III storage ring (DESY, Hamburg, Germany).[52,53] The synchrotron radiation wavelength (λ) and photon energy were 0.0957 nm and 13 keV, respectively. The X-ray impinged onto the sample under an incident angle of $\alpha_i = 0.35°$, which is well above the total reflection angles (critical angles) of all involved materials in the investigated hybrid film system. In this case, the X-ray beam penetrated the whole film, providing averaged scattering information from the full depth of the film. The scattering data were collected with a 2D detector (Pilatus 300 K Dectris Ltd., Switzerland, with 487 × 619 pixels, pixel size 172 × 172 μm^2). To access the desired nanostructure range, a sample–detector distance of 2.55 m was employed. For avoiding over-

saturation, two beam stops were placed in front of the detector in positions of the direct beam and the specular reflection, respectively. Structural information is extracted from horizontal (q_y direction, parallel to the sample surface) and vertical cuts (q_z direction, perpendicular to the sample surface) of the 2D intensity distribution.[54] For a deeper analysis, a model assuming a Lorentzian distribution of length scales was applied for fitting q_y profiles. The films were examined repeatedly along several locations on the sample within a distance of 5.0 mm to avoid possible X-ray beam induced effects to the films.

2.3.5. Magnetic Property Measurement System (MPMS). A superconducting quantum interference device (SQUID) magnetometer (MPMS XL-7, Quantum Design, San Diego, CA, U.S.A.) was employed to measure the magnetization as a function of temperature. All measurements were carried out while applying an external magnetic field from −500 to 500 mT in the film plane and repeated at different temperatures of 2, 5, 10, 20, 50, and 100 K.

3. RESULTS AND DISCUSSION

Hybrid films composed of the DBC PS-b-PNIPAM and PS-coated γ-Fe_2O_3 NPs were spin-coated from 1,4-dioxane solutions onto precleaned Si substrates. For the desired applications in magnetic storage devices and magnetic sensors, film homogeneity and uniformity are essential. Both are affected by the solution viscosity, which is controlled by the polymer concentration, in the film preparation via spin coating. At high friction, arising from high viscosities, inhomogeneous films result due to limited NP mobility. As observed in initial tests, a polymer concentration of the solution of 45 mg/mL gives macroscopically homogeneous hybrid films (corresponding optical microscopy data are not included).

3.1. Film Thicknesses. The film thickness increases linearly from 238 ± 2 nm to 264.9 ± 1.3 nm with increasing NP concentration from 0 to 15 wt %, as shown in Figure 1. Since all
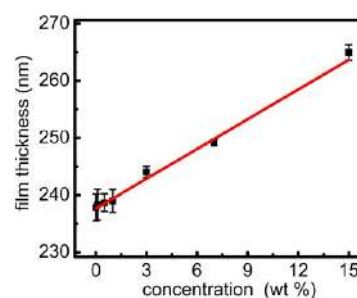
**Figure 1.** Thicknesses of γ-Fe_2O_3:PS-b-PNIPAM films measured as a function of the NP concentration (the solid line is a linear fit).

hybrid films were prepared using the identical protocol, the effect of added NPs on the viscosity of the solutions is fairly limited, and the temperature and relative humidity were constant during the thickness measurements, the film thickness expansion is caused by the volume of the incorporated NPs. Because a DBC film is confined between two different interfaces, different orientations of the microphase separation structure can result from such change in film thickness.[55−58]

3.2. Local Surface Morphology. For characterization of the surface morphology, the hybrid films are examined with SEM as a function of NP concentration. In these SEM measurements, the electron penetration depth is 10 nm. Figure 2 shows the corresponding gray scale SEM micrographs, in which the dark and bright areas corresponding to the PNIPAM and PS domains, respectively. The brightest randomly isolated distributed objects are maghemite NP aggregates. On the basis
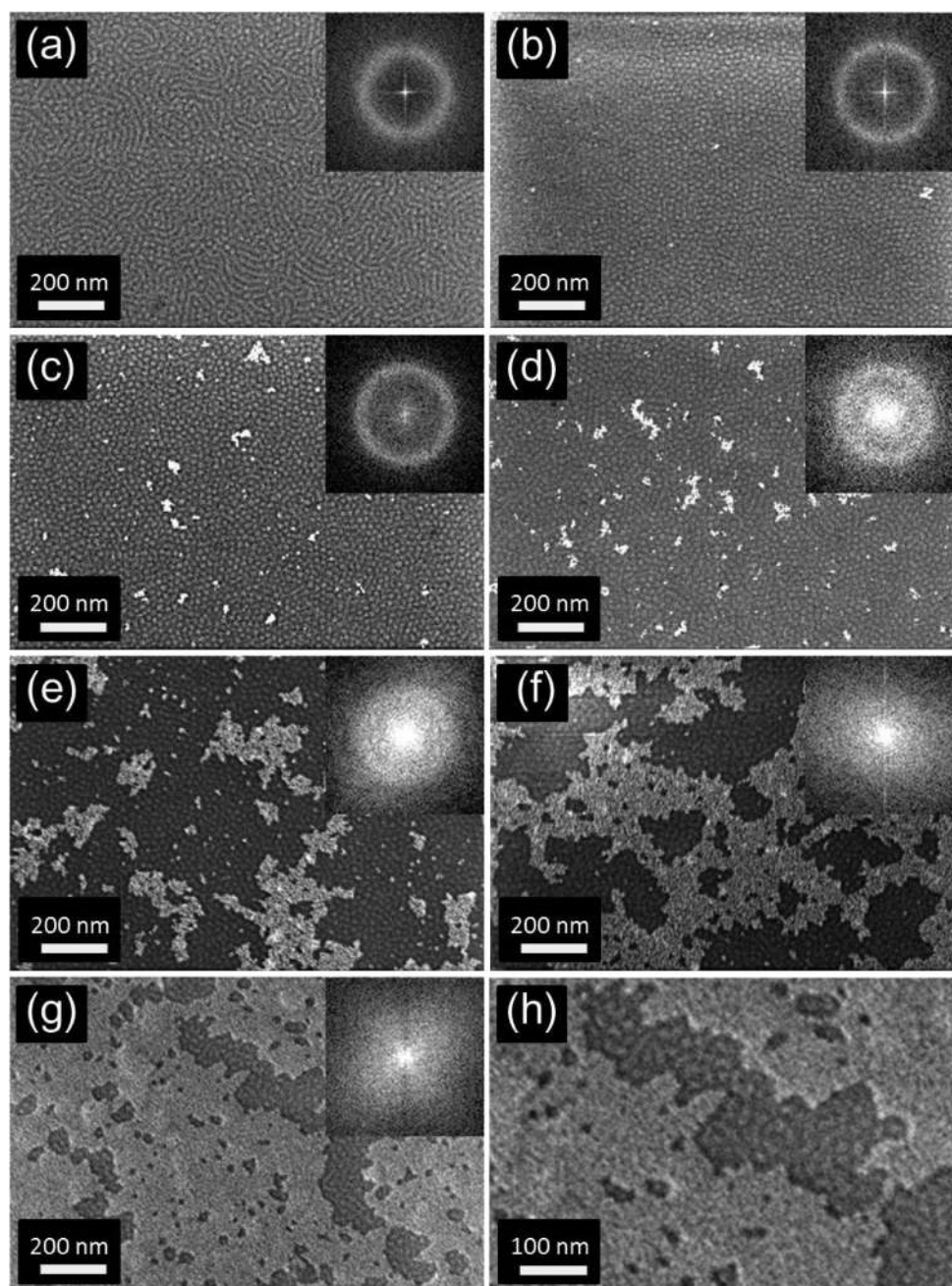
Figure 2. SEM micrographs showing the surface nanostructures of the hybrid films with different NP concentrations: (a) 0, (b) 0.1, (c) 0.5, (d) 1, (e) 3, (f) 7, (g) and (h) 15 wt %. To emphasize the nanostructure transition in the NP-aggregate free area, the image in (g) is magnified 2 times with a reduced scan size in (h). Insets show the 2D FFT patterns.

of self-consistent field theory,[17] a cylindrical morphology is expected for the investigated DBC PS-*b*-PNIPAM, due to the PS weight fraction of 0.34. For the NP-free DBC film, labyrinth-like, parallel cylinders with only small scattered areas having perpendicular cylinders (with respect to the film surface) are observed (Figure 2a). Such parallel-oriented microphase separated morphologies are favored for film thicknesses larger than the characteristic periodic distance of DBC.[30,59] In the current study, upon incorporation of NPs into the DBC matrix, at an extremely low NP concentration, the dominating parallel orientation significantly changes into a long-range, lateral order of perpendicularly oriented cylinders (Figure 2b). So far in the literature, the perpendicular orientation was most reported in case of using sophisticated

or special treated substrates, or in case of confined thin films with thicknesses smaller than DBC periodic distances.[60,61]

The observed morphological transition from a parallel to a perpendicular orientation of the microphase separated structure is attributed to the tuned interfacial energy via embedded NPs, which arises from a competition between the entropic and enthalpic terms in the hybrid film system in order to minimize the free energy density.[60] The surface modification of the maghemite NPs by PS coating energetically promotes the selective deposition of the NPs into the PS domains of the DBC at low NP concentrations.[36,62,63] In other words, the PS-coated NPs, which appear chemically identical to one of the DBC blocks (PS), will not enter the chemically incompatible PNIPAM domains, or distribute randomly inside the polymer

matrix.[26] Consequently, the order and homogeneity of the orientation of the hybrid films are both enhanced significantly. Some analogous observations that indicated an enhancement of the long-range order and a switch of the domain orientations upon incorporation of NPs in DBC films were reported previously.[2,30,33]

The degree of orientation of the microphase separated structure of the films is further enhanced at a slightly higher NP concentration (0.5 wt %, Figure 2c). In addition, the SEM micrograph contrast is also improved by higher NP incorporation. Thus, the selectivity of the deposited NPs into one or the other DBC domains arises as a significant factor regarding the fabrication of highly ordered, good perpendicularly oriented cylindrical morphologies.

However, at higher NP contents (>0.5 wt %), the long-range ordered morphology is undermined. NP-aggregates are formed and monotonically increase in size with increasing NP concentration (Figure 2d−g). The ability of the PS domains to accommodate NPs is limited due to the increase in the entropy cost. Upon higher NP upload, this limit is exceeded. Consequently, the excess NPs are squeezed out of the PS domains and accumulate at the film surface. At such NP concentrations, the hybrid system is dominated by the entropic penalty. The NPs favor aggregation, despite their surface coating, in agreement with Monte Carlo simulations at high NP concentrations within a host DBC matrix.[64,65] More NPs are accumulated, surrounding the initial small NP-aggregates, which impel the NP-aggregates to develop in a larger size. At NP concentration ≥7 wt %, the aggregates form network structures with a percolation path and cover large surface areas of the films. At NP concentrations of 3 and 7 wt %, a tendency of a morphological transition from perpendicular to parallel cylindrical orientation of the NPs/DBC hybrid film begins to gradually appear in the NP-aggregate free areas (Figure 2e,f). This gradual transition becomes even more pronounced at the highest investigated NP concentration (15 wt %, Figure 2g). For clarity, an interesting area of Figure 2g is further magnified and shown in Figure 2h. Although the excess NPs come to the film surface, part of them could contribute to an additional swelling of the PS domains, thereby expanding the PS domains anisotropically and causing a change in morphology.

For further investigating the surface order, the fast Fourier transformations (FFTs) of the SEM micrographs are used (insets in Figure 2). Isotropic rings are observed, which indicate that the surface structures are isotropically distributed with a fixed center-to-center domain spacing. As the NP concentration increases, the rings in the FFTs become narrower and more pronounced (≤0.5 wt %). At high NP concentrations (≥1 wt %), the rings broaden again until they vanish due to a large number of randomly distributed NP-aggregate networks.

For a quantitative analysis, the power spectral density (PSD) functions are extracted by azimuthal integration of the FFT data (Figure 3). The extracted intensities (Figure 3) exhibit an interesting change of the q position of the pronounced peak (marked with I in Figure 3), which represents the interdomain spacing on the DBC film surface. Upon addition of NPs, peak I shifts toward a higher q in case of 0.1 wt % NPs incorporation. This shift is not caused by a decrease of lateral distances between PS domains, but results from the geometry transition of the microphase separated structure, which differs for calculating of parallel cylinder ($d = 2\pi/q$) and perpendicular cylinder ($d = 4\pi/\sqrt{3}q$, for hexagonal lattice) from reciprocal space to real space.[66,67] The correspondingly calculated domain
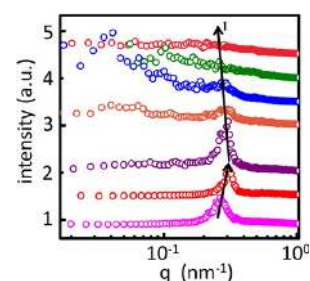

Figure 3. Power spectral density (PSD) functions extracted from azimuthal integration of the intensity distribution in the FFT patterns with different NP concentrations: 0, 0.1, 0.5, 1, 3, 7, and 15 wt %, from bottom to top. Peak I shows the q value of the lateral structure originated from microphase separation of the DBC. The PSD profiles are shifted along y axis for clarity.

spacings, D, are 23.7 ± 0.1 nm (without NPs using $D = 2\pi/q$) and 23.8 ± 0.1 nm (with NPs using $D = 4\pi/\sqrt{3}q$), respectively. Further, the q position of peak I decreases with increasing NP concentration from 0.1 to 3 wt %, which corresponds to an expansion of the domain distances from 23.8 to 26.2 nm. In addition, the width of peak I is initially narrower and broadens with increasing NP concentration, revealing an initial increase in order, followed by a decay in order. At high NP concentrations, peak I is hardly observed, and its position is ill-defined.

However, SEM provides only 2D information on the film surface structure, whereas the topography information is not accessible. To probe the topography, AFM data were measured. Figure 4 shows AFM data for selected samples: NP-free DBC film (Figure 4a) and hybrid film with 15 wt % NPs loading (Figure 4b). One has to note that compared with SEM images, the detected contrast in the AFM measurements is different.

In Figure 4a, curved stripe-shaped parallel cylindrical nanostructures, originating from the microphase separation and self-assembly of the DBC film can be observed. In contrast, Figure 4b shows a different topography. At high NP concentrations (15 wt %), worm-like cylinders are well observed in the NP-aggregate free surface areas, whereas the majority of the film surface is covered with NP-aggregates. The height (peak-to-valley amplitude) profiles are demonstrated by representative line cuts provided in the Supporting Information (SI Figures S1). Line cuts collected from 3 randomly selected positions are shown with colored dotted lines in Figure 4a,b. The local height modulations of the NP-free DBC are confined within an amplitude of less than 1 nm (Figure S1a), whereas the mean height differences on larger scale are on the order of 5 nm. At high NP loading, the mean height differences increase to more than 11 nm, with local height differences staying small (SI Figure S1b). This increase in mean height differences is caused by the NPs. The result indicates that, besides the well pronounced NP-aggregates found on the film surface, partially embedded NP-aggregates might occur inside the DBC film. Furthermore, 2D FFT patterns of these AFM topography images and their power spectral density (PSD) functions are provided in the SI (Figure S2). The observations from the FFT and PSD analysis are consistent with the corresponding results of SEM data analysis. In addition, the root-mean-square (rms) roughness values are calculated from the AFM micrographs. On the local scale, for the NP-free DBC film, the rms roughness is approximately 0.6 nm. With incorporation of 15 wt % NPs, the
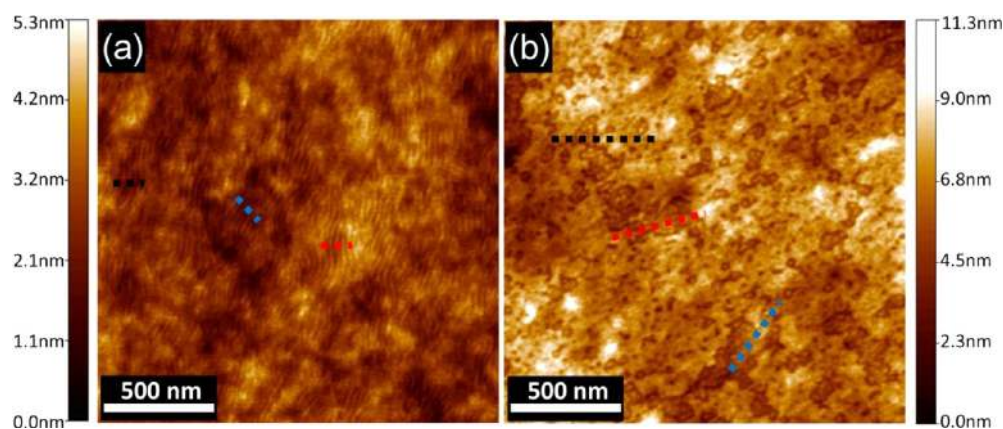
Figure 4. AFM topography images of (a) NP-free DBC film and (b) metal oxide/DBC hybrid film with NP concentration of 15 wt %. The dotted lines indicate line cuts shown in the Supporting Information.

rms roughness increases due to the presence of the large NP-aggregates, but remains below 2 nm.

3.3. Inner Film Morphology. Since AFM and SEM provide only information on the surface morphology of the metal oxide-DBC hybrid films, but the magnetic properties will depend on the inner film morphology as well, grazing incidence small-angle X-ray scattering (GISAXS) experiments were performed. GISAXS provides an excellent statistical relevance over a macroscopic illuminated sample area with respect to the structure sizes, size distributions and spatial correlations. Details about the GISAXS technique are reported elsewhere.[54]

Figure 5 shows 2D GISAXS data of hybrid films with different NP concentrations. For all measurements, the most intense specular reflection is blocked by a beamstop for protecting the detector from oversaturation, and the position of that is well separated from the material characteristic Yoneda peak. Thus, characteristic features, such as the Yoneda peak and intensity modulations are easily distinguished on the 2D detector. In general, the significant changes of the GISAXS data appear with incorporation of different amounts of NPs.

3.3.1. Vertical Structures. Already in the 2D GISAXS data of samples with a high NP concentration (≥ 3 wt %), an intensity modulation along the q_z direction is seen (Figure 5d–f). Such an intensity modulation results from a partial phase coherence of the X-ray waves diffusely scattered from different interfaces, which causes increase in intensity in a sheet in reciprocal space.[41] Compared with the results from film surface measurements using SEM and AFM, the most probable source of the mentioned partial phase coherence of diffusely scattered wave is the correlated roughness of the large NP-aggregates enrichment layers on top of the hybrid films. In other words, the correlated roughness arises from a locally long-range correlated layer thickness between two adjacent interfaces of the hybrid film/NP-aggregates and NP-aggregates/air. Therefore, the intensity modulation along the q_z direction indicates that the NP enrichment layer has a nearly uniform thickness with only small variances.[68]

For further quantitative analysis, vertical line cuts of the 2D GISAXS data are made at $q_y = 0$ and presented in Figure 6a. The thickness of the correlated enrichment NP-aggregates layer, d, is determined by a simple approach of the distance between adjacent minimal intensity (marked by dashed lines in Figure 6a): $d = 2\pi/\Delta q_z$. Therefore, with $\Delta q_z = 1.13$ nm^{-1}, d is 5.6 ± 0.1 nm, perfectly agreeing with the AFM observations. Similar roughness correlations were reported in several other
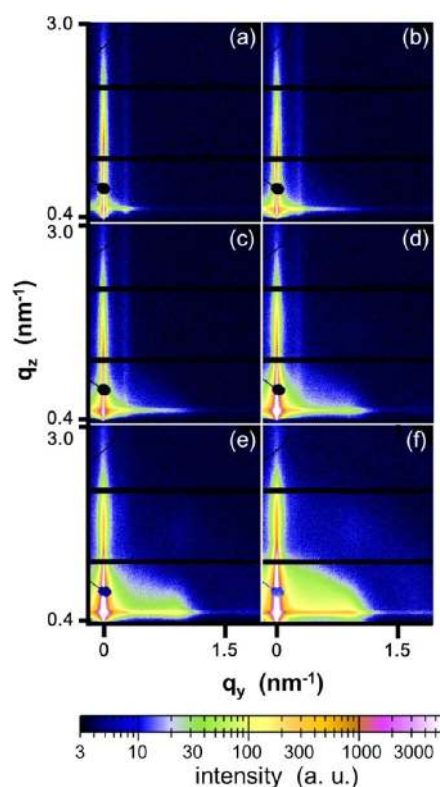
Figure 5. Selected 2D GISAXS data of metal oxide-DBC hybrid films with different NP concentrations: (a) 0, (b) 0.5, (c) 1, (d) 3, (e) 7, and (f) 15 wt %. All data are displayed with the same intensity adjustments in logarithmic scale. The horizontal black lines are the insensitive detector areas between modules.

polymer systems, consisting either of a single layer or of complex multilayer films.[69,70]

To extract further information, vertical line cuts are also extracted at different q_y values different from zero. The obtained off-center line cuts are exemplified for the hybrid film with 15 wt % NP in Figure 6b. The used increment in q_y direction is $\Delta q_y = 1.77 \times 10^{-2}$ nm^{-1} (from the top to the bottom). The intensity of the resonant diffuse scattering along the q_z direction decreases with increasing q_y values (along the arrow direction in Figure 6b), implying the absence of vertical structural correlation at certain q_y values. Treating the roughness spectrum of the hybrid film/NP-aggregates interface as a
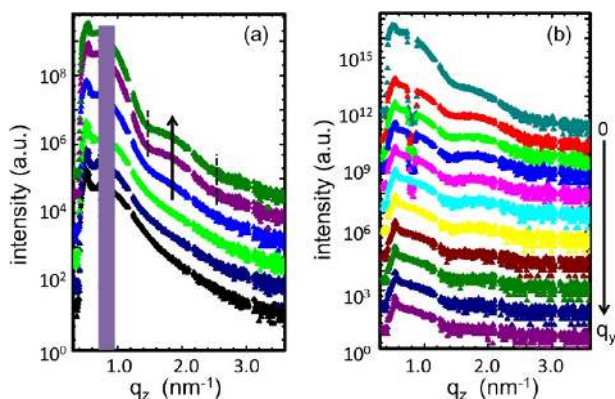
Figure 6. (a) Vertical line cuts (q_z) of the 2D GISAXS data of the hybrid films at $q_y = 0$ for films with different NP concentrations (0, 0.5, 1, 3, 7, and 15 wt % from bottom to top). Dashed lines and arrow mark the characteristic intensity modulation. (b) Vertical line cuts (q_z) for a selected hybrid film with a NP concentration of 15 wt % at different q_y positions (0 to 0.177 nm^{-1} from top to bottom as indicated by the arrow, using an increment of $\Delta q_y = 1.77 \times 10^{-2}$ nm^{-1}) showing the decay of the interference fringe of the resonant diffuse scattering. All curves are shifted along y-axis for clarity.

reference, a characteristic decay length of the roughness correlation can be defined, yielding a critical cutoff in-plane length scale (R_c).[71] At $R < R_c$, an individual roughness spectrum is installed independent of the underlying hybrid film/NP-aggregates interface.[40] At $R > R_c$, the morphology of the hybrid film/NP-aggregates interface can be replicated by the NP-aggregates enrichment layer. Within the experimental errors, a value of $R_c = 35.5$ nm is determined from the corresponding off-centered vertical line cuts. The R_c value is slightly larger than the lateral periodic distance (30.0 nm), which will be discussed in detail in the following section.

Thus, the observed thin NP-aggregates enrichment layer has a mean thickness of 5.6 nm and replicates the topography of the underlying film surface when the in-plane structural sizes are larger than 35.5 nm. Since this thickness value is smaller than the mean NP diameter, it is likely that the NPs are embedded to a certain extent inside the top part of the DBC film.

3.3.2. Lateral Structures. Already in the 2D GISAXS data of the samples, information about lateral structural is clearly seen. In the case of the NP-free pure DBC film (0 wt %, Figure 5a), a pronounced side peak is observed, which arises from the presence of well-ordered cylindrical domains due to the difference in electron density contrast between PS and PNIPAM. Upon the incorporation of NPs at low concentration (≤ 1 wt %, Figure 5b,c), the intensity of the side peak and Yoneda region becomes more intense, because of the enhanced order and improved electron density contrast originating from the NPs inside the PS block of the DBC. With further NP loading, the side peak decays and vanishes finally at the highest concentration (15 wt %, Figure 5f) due to the intensive scattering of a large amount of NPs dominating the scattering pattern. In addition, a second side peak appears at a NP concentration of 3 wt % (Figure 5d), which becomes more pronounced with increasing NP concentration. It originates from the structure factor of closely packed NPs in the NP-aggregates and provides information about the NP size.

For further analysis, horizontal line cuts from the 2D GISAXS data are performed at a fixed q_z value, equivalent to the critical angle of the DBC ($q_{z,c} = 0.51$ nm^{-1}), and shown in

Figure 7a. Three characteristic main features are found in these line cuts and denoted as peaks in the following (marked with
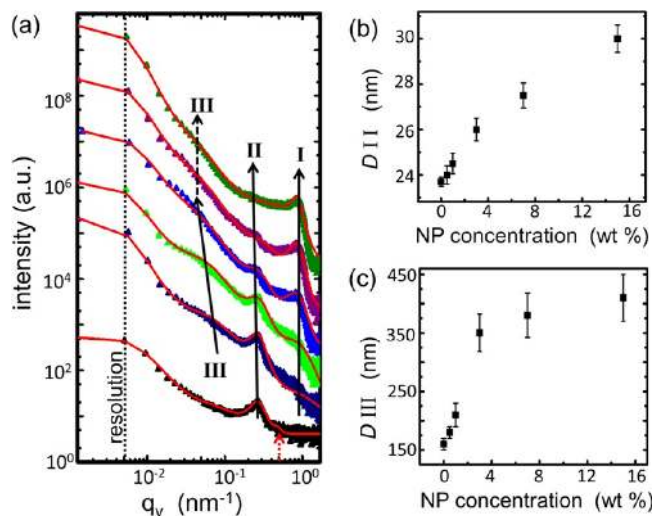
Figure 7. (a) Horizontal line cuts (q_y) of the 2D GISAXS data of the hybrid films with different NP concentrations (0, 0.5, 1, 3, 7, and 15 wt % from bottom to top). The q_y profiles are shifted along y-axis for clarity and presented as symbols along together with the fits (red solid line). Characteristic features are indicated: Peak I (contribution of metal oxide NPs), peak II (periodic distance of microphase separation structure of DBC), and peak III (characteristic NP-aggregates distance). The red dotted arrow in the bottom part shows the second-order peak II. Extracted values of (b) the microphase separation structure DII and of (c) NP-aggregates distance DIII as a function of NP concentration.

arrows and labeled I, II, and III in Figure 7a. The peak denoted with I is located at a higher q_y value of 0.86 nm^{-1} and shows up in the GISAXS data only for films with incorporated NPs. At low NP loading, peak I arises from the form factor contribution of metal oxide NPs and has a broad shoulder-like shape. At higher NP concentrations (≥ 3 wt %), the broad peak I becomes more prominent, since it is now caused by a structure factor of closely packed NPs. Its position is independent of the NP concentration and a diameter of spherical NPs of 6.5 ± 0.5 nm is extracted from the fit to the data, which matches the mean NP diameter. This phenomenon was already observed in similar experiments featuring iron oxide NP doping on organic matrices.[72] Peak II, which corresponds to the upright side maximum in the 2D GISAXS patterns (in Figure 5), is located at smaller q_y values. It represents the highly ordered arrangement of cylindrical PS domains of the DBC film. Peak II is most pronounced at low NP concentrations and becomes less pronounced with higher NP load, nearly vanishing at a high NP concentration of 15 wt %. The q_y position of peak II reveals the distance between two neighboring PS cylindrical domains originating from the microphase separation of the DBC. A Lorentzian distribution of length scales was applied for modeling this structure factor during the fitting procedure and the resolution was modeled by a Lorentzian-shaped resolution function. In the case of the NP-free DBC film, a low-intensity second-order peak (marked with red dotted arrow in Figure 7a) is visible due to the rather well ordered nanostructures. The corresponding in-plane lengths of the first and second order peaks II are 23.7 and 13.1 nm, respectively. The ratio of their q_y value is $0.553 \approx 1 : \sqrt{3}$, which matches the
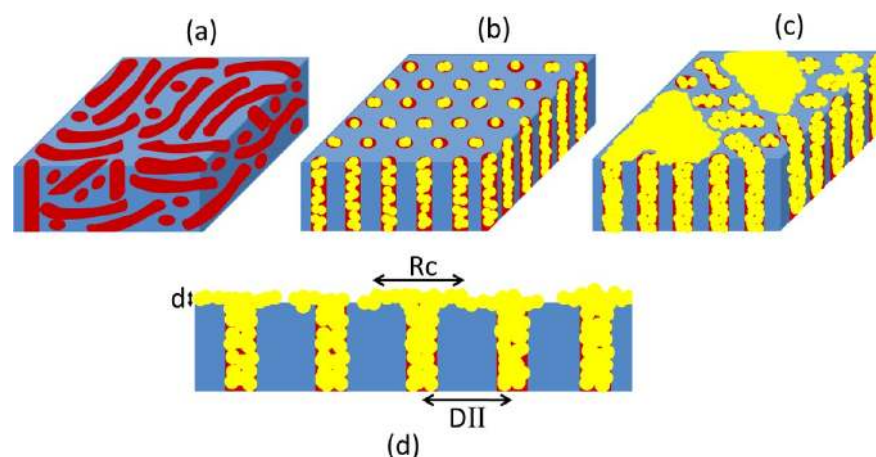
Figure 8. Illustration of the morphological evolution of films for (a) the NP-free pure DBC template, incorporation with (b) low, and (c) high concentrations of NPs. (d) Cross sectional sketch of the NP-aggregates enrichment layer for hybrid film at high NP concentrations; PS domains (red), PNIPAM domains (blue), and NPs (yellow). R_c, d, and DII represent critical cutoff in-plane length scale, thickness of NP-aggregates enrichment layer and periodic distance of DBC, respectively.

assumption of a cylindrical geometry. Therefore, inside the NP-free DBC film, highly ordered, hexagonally packed, cylindrical PS domains are dispersed in a PNIPAM matrix. As seen in Figure 7a, upon increasing NP concentration (from 0 wt % to 15 wt %) the position of peak II shifts toward smaller q_y values resulting from an increase in the lateral spacing between PS domains. The corresponding periodic distance, DII, increases from 23.7 ± 0.2 nm to 30.0 ± 0.6 nm (Figure 7b). The expansion of the periodic distance is caused by the selective swelling of the PS domains upon incorporation of the NPs. In case of a tiny amount of NPs (0.5 wt %), the fwhm of peak II becomes narrower, which implies an enhancement of the structural order. The absence of a second order peak, which would be expected at higher structural order, is caused by the additional scattering originating from the form factor of the embedded NPs. With further increase in NP concentration, peak II becomes less pronounced and broader, which reveals the oversaturation of the PS domains with NPs. This oversaturation perturbs the initially established long-range order structure of the hybrid films.

An additional broad shoulder-like scattering feature (peak III) appears at even smaller q_y values. It is attributed to the NP-aggregates center-to-center distance. As the sizes of these NP-aggregates increases, the inter NP-aggregates spacing increases. Thus, this peak indirectly refers to the pronounced increase of aggregate sizes upon NP upload. As seen in Figure 7a, peak III initiates with the incorporation of NPs, and shifts in position with increasing NP concentration. With the increase of NP concentration from 0.5 to 3 wt %, the corresponding characteristic NP-aggregates distance, DIII, extracted from the fitting shows a linear increase from 180 ± 10 nm to 380 ± 25 nm with a large distribution (in Figure 7c). This indicates randomly dispersed large structures. Given the NP concentration ≥7 wt % (in Figure 7a), the scattering intensity at low q values is very broad and the early observed peak (peak III, marked with dashed arrow) is only weakly pronounced, indicating large interparticle distance distributions and a relatively more ill-defined large size NP-aggregates at high NP concentrations. These results are in agreement with SEM data where large sized interconnected NP-aggregates at NP concentrations ≥7 wt % are observed (see Figure 2f,g).

In addition, the variation tendencies of the peak (I, II, and III) widths (full width half-maximum, fwhm), which reveal the systematic order of the nanostructure, are presented in the SI (Figure S3). Upon the NP load, the widths of peak I and peak II obviously become narrower or broader, respectively. However, the width of peak III has larger amplitude but changes slightly with the increase of the incorporated NPs.

3.3.3. Film Morphology. The film morphology as determined from both, real-space and reciprocal space investigations, is shown in Figure 8.

The changes in the nanostructures of the hybrid films upon incorporation of NPs are illustrated for the case of low and high NP concentration. Due to self-assembly, the microphase separated structure of the NP-free DBC film, which serves as template for the NP incorporation, is composed of cylindrical PS domains homogeneously distributed in a PNIPAM continuous matrix. With respect to the film surface, the PS domains exhibit a preferential parallel orientation (Figure 8a). This parallel orientation of the PS cylinders can be ascribed mainly to two origins: One is the interfacial preference arising from a lower surface energy, which makes the PS domains to have an affinity to air in comparison to the PNIPAM domain. Another is that the surface boundary condition predicting a parallel morphology is prone to be achieved, given the film thickness is far above the polymer periodic distance.[56,73] Since the film thickness is 237 nm, it by far exceeds the DBC periodic distance of 23.7 nm.

At low NP concentrations (Figure 8b), the preferential interaction between the NPs and the PS domains drives NPs selectively well distributed into the PS domains. In this case, the original interfacial energies of the film/air and segment-to-segment Flory−Huggins interaction parameter are modified due to the embedded NPs. This causes a change in the orientation of the cylindrical NP/PS domains from parallel to perpendicular with respect to the film surface. The spacing of neighboring PS domains increases slightly due to the preferential incorporation of NPs. At low NP concentrations, the enthalpic contribution is enhanced, which leads to a more ordered morphology.

At high NP concentrations (Figure 8c), the long-range ordered structures remain only to some extent, and large NP-aggregates are formed. On the one hand, the former highly

ordered PS cylinders have been stretched heavily and deformed to accommodate more NPs inside. On the other hand, the excessive amount of NPs, which can no longer be accommodated inside the PS cylinders, are located on the film surface and NP-aggregates end up forming a layer. This NP-aggregate layer has a mean thickness which is slightly smaller than the diameter of the NPs, which can be a sign that it is to some extent embedded in the film (Figure 8d). The roughness features of the lower interface of hybrid film/NP-aggregates is replicated by the NP-aggregates layer for in-plane structure size $R > R_c$. The determined value of R_c is slightly larger than the neighboring PS domain spacing (DII).

3.4. Magnetic Properties. The magnetic behavior of the metal oxide-DBC hybrid films is probed by magnetization measurements using external magnetic fields from −500 to 500 mT, applied in the film plane. The effect of NP concentration on the magnetic properties of hybrid films at 2 K is shown in Figure 9a. For a quantitative analysis, the NP concentration-
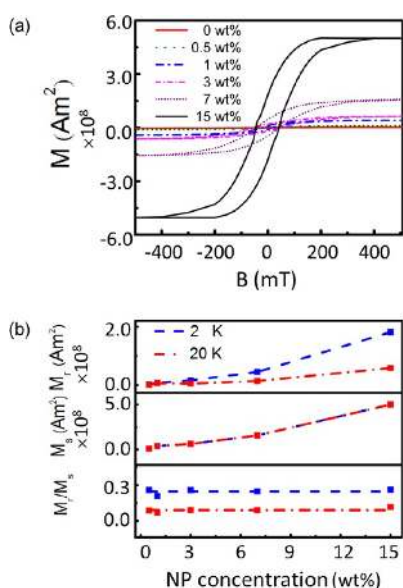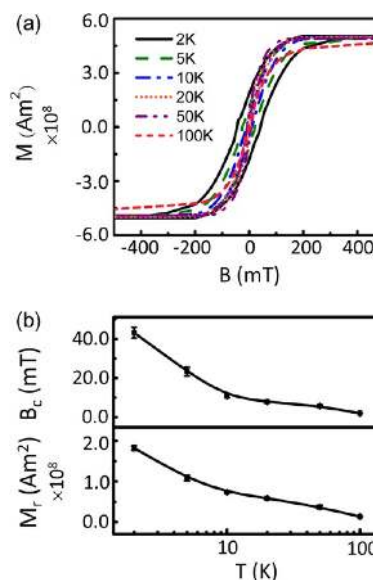

Figure 9. (a) Magnetic moments measured as a function of external magnetic fields at 2 K for hybrid films for different NP concentrations as indicated in the figure. (b) Remanence, M_r, saturation magnetization, M_s, and relative remanence, M_r/M_s extracted from the corresponding measured magnetic moments at 2 K (blue dashed line) and 20 K (red dashed-dotted line), respectively.

dependent remanence, M_r, saturation magnetization, M_s, and relative remanence, M_r/M_s at 2 K are extracted. They are presented in Figure 9b. For comparison, data measured at 20 K are also included. Within experimental errors, M_r and M_s show the similar tendency for both temperatures. Both increase evenly with increasing NP concentration, and in consequence, the ratio M_r/M_s is independent of the NP concentration. Such independence of M_r/M_s of the NP concentration was already observed in earlier investigations on other DBC films with embedded iron oxide nanoparticles.[33,36,74] Additional magnetic moment curves have been measured for selected hybrid films at the same conditions, but with applied external magnetic fields rotated by 90° in the film plane, but no magnetical anisotropy was observed. In earlier works using an ordered DBC matrix with nano- and micro NP-aggregate wires, which exhibit an anisotropic orientation, a dependence of the orientation of the magnetic field was found.[36] Therefore, in the present sample we

find an isotropic NP distribution in lateral direction. Thus, the presence of the NP aggregates has no influence on the magnetic behavior in terms of magnetic isotropy. This is beneficial for applications, since no special alignment of the sample with respect to the magnetic field needs to be done.

In Figure 10, the temperature-dependent magnetic behavior is shown for a selected hybrid film with a NP concentration of

Figure 10. Selected hybrid film with 15 wt % NP concentration: (a) Magnetic moments measured as a function of applied external magnetic fields at different temperatures; (b) Coercivity, B_c, and remanence, M_r, extracted from the measured magnetic moments at different temperatures. The solid lines are guides to the eye.

15 wt %. The width of the hysteresis loop decreases with increasing temperature, in agreement with previous investigations.[33,36,74,75] However, some dissimilarities are found. In our previous study, for hybrid films of a perforated lamellar nanostructure established by DBC with identical type and amount of maghemite NPs, a temperature dependent maximum magnetization was observed even with a higher external magnetic field (700 mT).[33] In contrast, the current study exhibits a different temperature independent saturation magnetization with an even lower external magnetic field (500 mT) due to a more highly ordered, well oriented film morphology. However, for the measurement at a relatively high temperature of 100 K, the present employed external magnetic fields are not large enough to saturate magnetization. This observation keeps consistent with Curie's law.[76] As the temperature rises, hysteresis loops superimpose, but become narrower and approach to zero, which is the fingerprint of a typical superparamagnetic behavior. The extracted coercivity provides a more precise value of the half hysteresis (Figure 10b). The coercivity strongly decreases with the temperature and vanishes when the temperature exceeds a specific blocking temperature of involved superparamagnetic NPs. This temperature T is defined by the integrated Néel−Brown formula:[77,78]

$$\tau = \tau_0 \exp\left(\frac{KV}{K_B T}\right) \tag{1}$$

where τ is the relaxation time, τ_0 of 10^{-10} s is the inverse attempt frequency, and KV represents the activation energy. In

addition, the remanence shows a sharp decay with the increase in temperature as well (in Figure 10b), which is distinguished from a more moderate decay shown in our previous investigation from a randomly oriented DBC with widely distributed maghemite NPs.[75] Both the temperature-dependent decay behaviors of coercivity and remanence are attributed to thermal fluctuations.

Considering all aspects of the magnetic behavior, the investigated hybrid films exhibit the typical superparamagnetic properties and are consistent with a modified model of Stoner−Wohlfarth−Néel. This model, based on the developed thermodynamics of superspins was modified by an elastic torsion mechanism.[74,79] The present observations interestingly differ from the previous studies, which used other DBC templates with incorporated maghemite NPs.[36,75] Therefore, the observed magnetic behavior is in close relation to the morphology of the hybrid film system.

4. CONCLUSIONS

The structure of metal oxide NPs/DBC hybrid films, consisting of PS-coated γ-Fe$_2$O$_3$ NPs and PS-b-PNIPAM DBC, has been investigated with surface profilometry, SEM, AFM, and GISAXS at a range of varied NP concentrations and the morphology has been related to the magnetic behavior. The arrangement of the NPs, guided by the cylindrical PS domains of the DBC template, is realized via the preferential incorporation of the surface modified NPs. An unusual parallel-to-perpendicular orientation transition of the microphase separated structure is observed. Moreover, the enthalpic contribution is also modified by the presence of highly dispersed, selectively embedded NPs in the low concentration range. This results in the enhancement of nanostructure order and orientation. Such a well-ordered, perpendicularly oriented cylindrical nanomorphology of the hybrid films is fabricated via a wet chemical self-assembly method, by a simple and highly reproducible spin coating procedure without any pre- or post-treatment steps. The periodic distance of DBC domains increases to accommodate the NPs. At higher NP concentrations, the previous long-range ordered structures are mostly lost. The overload of NPs leads to the formation of large NP aggregates on the film surface. With further increase in NP concentration a network of NP-aggregates representing an enrichment layer on the film surface is observed. At all NP concentrations, the superparamagnetic behavior of the hybrid films is confirmed. Thus, the excess NPs in the surface layer have no negative influence on the magnetic behavior.

We conclude, that with an appropriate selection of the weight ratios of NPs versus DBC, varied ordered morphological hybrid films with different structural emphasis can be established in a simple and low cost preparation process for versatile potential applications. This may be especially useful in the fields of high density magnetic storage media and thermoresponsive magnetic sensors. Based on the understanding of the morphology of γ-Fe$_2$O$_3$:PS-b-PNIPAM films further studies can address the humidity-dependent swelling, thermo-responsible switching, and humidity-dependent magnetic properties of the metal-oxide DBC hybrid nanocomposite films.

ASSOCIATED CONTENT

Ⓢ Supporting Information

1. Local Surface Morphology: (Figure S1) representative line cuts from the AFM micrographs; (Figure S2) 2D FFT patterns of AFM topography images. 2. Evolution of the Relative Amplitudes in the GISAXS Data: (Figure S3) full width at half maxima (FWHM) obtained from the fits of the horizontal line cuts. The Supporting Information is available free of charge on the ACS Publications website at DOI: 10.1021/acsami.5b03308.

AUTHOR INFORMATION

Corresponding Author

*Phone: +49 89 289 12451. Fax: +49 89 289 12 473. E-mail: muellerb@ph.tum.de.

Notes

The authors declare no competing financial interest.

REFERENCES

(1) Ganesan, V.; Jayaraman, A. Theory and Simulation Studies of Effective Interactions, Phase Behavior and Morphology in Polymer Nanocomposites. *Soft Matter* **2014**, *10*, 13−38.

(2) Lin, Y.; Böker, A.; He, J.; Sill, K.; Xiang, H.; Abetz, C.; Li, X.; Wang, J.; Emrick, T.; Long, S.; Wang, Q.; Balazs, A.; Russell, T. P. Self-Directed Self-Assembly of Nanoparticle/Copolymer Mixtures. *Nature* **2005**, *434*, 55−59.

(3) Bockstaller, M. R.; Mickiewicz, R. A.; Thomas, E. L. Block Copolymer Nanocomposites: Perspectives for Tailored Functional Materials. *Adv. Mater.* **2005**, *17*, 1331−1349.

(4) Huber, D. L. Synthesis, Properties, and Applications of Iron Nanoparticles. *Small* **2005**, *1*, 482−501.

(5) Wei, Q.; Lin, Y.; Anderson, E. R.; Briseno, A. L.; Gido, S. P.; Watkins, J. J. Additive-Driven Assembly of Block Copolymer-Nanoparticle Hybrid Materials for Solution Processable Floating Gate Memory. *ACS Nano* **2012**, *6*, 1188−1194.

(6) Black, C. T.; Murray, C. B.; Sandstrom, R. L.; Sun, S. Spin-Dependent Tunneling in Self-Assembled Cobalt-Nanocrystal Superlattices. *Science* **2000**, *290*, 1131−1134.

(7) Gu, H.; Ho, P.-L.; Tsang, K. W. T.; Wang, L.; Xu, B. Using Biofunctional Magnetic Nanoparticles to Capture Vancomycin-Resistant Enterococci and Other Gram-Positive Bacteria at Ultralow Concentration. *J. Am. Chem. Soc.* **2003**, *125*, 15702−15703.

(8) Lu, A.-H.; Salabas, E. L.; Schüth, F. Magnetic Nanoparticles: Synthesis, Protection, Functionalization, and Application. *Angew. Chem., Int. Ed.* **2007**, *46*, 1222−1244.

(9) Park, S.; Lee, D. H.; Xu, J.; Kim, B.; Hong, S. W.; Jeong, U.; Xu, T.; Russell, T. P. Macroscopic 10-Terabit-per-Square-Inch Arrays from Block Copolymers with Lateral Order. *Science* **2009**, *323*, 1030−1033.

(10) Jang, Y. H.; Xin, X.; Byun, M.; Jang, Y. J.; Lin, Z.; Kim, D. H. An Unconventional Route to High-Efficiency Dye-Sensitized Solar Cells via Embedding Graphitic Thin Films into TiO$_2$ Nanoparticle Photoanode. *Nano Lett.* **2011**, *12*, 479−485.

(11) Kortaberria, G.; Arruti, P.; Mondragon, I.; Vescovo, L.; Sangermano, M. Dynamics of in Situ Synthetized Silver-Epoxy Nanocomposites as Studied by Dielectric Relaxation Spectroscopy. *J. Appl. Polym. Sci.* **2011**, *120*, 2361−2367.

(12) Kätelhön, E.; Compton, R. G. Nanoparticles in Sensing Applications: On What Timescale Do Analyte Species Adsorb on the Particle Surface? *Analyst* **2014**, *139*, 2411−2415.

(13) Lu, A. H.; Salabas, E. e. L.; Schüth, F. Magnetic Nanoparticles: Synthesis, Protection, Functionalization, and Application. *Angew. Chem., Int. Ed.* **2007**, *46*, 1222−1244.

(14) Sarkar, B.; Alexandridis, P. Block Copolymer-Nanoparticle Composites: Structure, Functional Properties, and Processing. *Prog. Polym. Sci.* **2015**, *40*, 33−62.

(15) Haryono, A.; Binder, W. H. Controlled Arrangement of Nanoparticle Arrays in Block-Copolymer Domains. *Small* **2006**, *2*, 600−611.

(16) Warren, S. C.; Messina, L. C.; Slaughter, L. S.; Kamperman, M.; Zhou, Q.; Gruner, S. M.; DiSalvo, F. J.; Wiesner, U. Ordered Mesoporous Materials from Metal Nanoparticle-Block Copolymer Self-Assembly. *Science* **2008**, *320*, 1748−1752.

(17) Hamley, I. W., Ed. *Developments in Block Copolymer Science and Technology*, 1st ed; John Wiley & Sons, Ltd: West Sussex, 2004.

(18) Hoheisel, T. N.; Hur, K.; Wiesner, U. B. Block Copolymer-Nanoparticle Hybrid Self-Assembly. *Prog. Polym. Sci.* **2015**, *40*, 3−32.

(19) Darling, S. B.; Yufa, N. A.; Cisse, A. L.; Bader, S. D.; Sibener, S. J. Self-Organization of FePt Nanoparticles on Photochemically Modified Diblock Copolymer Templates. *Adv. Mater.* **2005**, *17*, 2446−2450.

(20) Darling, S. B.; Bader, S. D. A Materials Chemistry Perspective on Nanomagnetism. *J. Mater. Chem.* **2005**, *15*, 4189−4195.

(21) Herzog, G.; Benecke, G.; Buffet, A.; Heidmann, B.; Perlich, J.; Risch, J. F. H.; Santoro, G.; Schwartzkopf, M.; Yu, S.; Wurth, W.; Roth, S. V. In Situ Grazing Incidence Small-Angle X-Ray Scattering Investigation of Polystyrene Nanoparticle Spray Deposition onto Silicon. *Langmuir* **2013**, *29*, 11260−11266.

(22) Metwalli, E.; Krisch, I.; Markovits, I.; Rawolle, M.; Ruderer, M. A.; Guo, S.; Wyrzgol, S.; Jentys, A.; Perlich, J.; Lercher, J. A.; Müller-Buschbaum, P. Polymer-Coated PtCo Nanoparticles Deposited on Diblock Copolymer Templates: Chemical Selectivity versus Topographical Effects. *ChemPhysChem* **2014**, *15*, 2236−2239.

(23) Zhao, Y.; Thorkelsson, K.; Mastroianni, A. J.; Schilling, T.; Luther, J. M.; Rancatore, B. J.; Matsunaga, K.; Jinnai, H.; Wu, Y.; Poulsen, D.; Fréchet, J. M. J.; Alivisatos, A. P.; Xu, T. Small-Molecule-Directed Nanoparticle Assembly towards Stimuli-Responsive Nanocomposites. *Nat. Mater.* **2009**, *8*, 979−985.

(24) Darling, S. B. Mechanism for Hierarchical Self-Assembly of Nanoparticles on Scaffolds Derived from Block Copolymers. *Surf. Sci.* **2007**, *601*, 2555−2561.

(25) Lo, C.-T.; Lee, B.; Pol, V. G.; Dietz Rago, N. L.; Seifert, S.; Winans, R. E.; Thiyagarajan, P. Effect of Molecular Properties of Block Copolymers and Nanoparticles on the Morphology of Self-Assembled Bulk Nanocomposites. *Macromolecules* **2007**, *40*, 8302−8310.

(26) Kim, B. J.; Chiu, J. J.; Yi, G. R.; Pine, D. J.; Kramer, E. J. Nanoparticle-Induced Phase Transitions in Diblock-Copolymer Films. *Adv. Mater.* **2005**, *17*, 2618−2622.

(27) Zhang, Q.; Gupta, S.; Emrick, T.; Russell, T. P. Surface-Functionalized CdSe Nanorods for Assembly in Diblock Copolymer Templates. *J. Am. Chem. Soc.* **2006**, *128*, 3898−3899.

(28) Lo, C.-T.; Lin, W.-T. Effect of Rod Length on the Morphology of Block Copolymer/Magnetic Nanorod Composites. *J. Phys. Chem. B* **2013**, *117*, 5261−5270.

(29) Lo, C.-T.; Chang, Y.-C.; Wu, S.-C.; Lee, C.-L. Effect of Particle Size on the Phase Behavior of Block Copolymer/Nanoparticle Composites. *Colloids Surf., A* **2010**, *368*, 6−12.

(30) Lauter-Pasyuk, V.; Lauter, H.; Gordeev, G.; Müller-Buschbaum, P.; Toperverg, B.; Petry, W.; Jernenkov, M.; Petrenko, A.; Aksenov, V. Parallel and Perpendicular Lamellar Phases in Copolymer−Nanoparticle Multilayer Structures. *Phys. B* **2004**, *350*, E939−E942.

(31) Lauter-Pasyuk, V.; Lauter, H.; Gordeev, G.; Müller-Buschbaum, P.; Toperverg, B.; Jernenkov, M.; Petry, W. Nanoparticles in Block-Copolymer Films Studied by Specular and Off-Specular Neutron Scattering. *Langmuir* **2003**, *19*, 7783−7788.

(32) Lauter-Pasyuk, V.; Lauter, H.; Ausserre, D.; Gallot, Y.; Cabuil, V.; Kornilov, E.; Hamdoun, B. Effect of Nanoparticle Size on the Internal Structure of Copolymer−Nanoparticles Composite Thin Films Studied by Neutron Reflection. *Phys. B* **1998**, *241−243*, 1092−1094.

(33) Yao, Y.; Metwalli, E.; Moulin, J.-F.; Su, B.; Opel, M.; Müller-Buschbaum, P. Self-Assembly of Diblock Copolymer−Maghemite Nanoparticle Hybrid Thin Films. *ACS Appl. Mater. Interfaces* **2014**, *6*, 18152−18162.

(34) Abul Kashem, M. M.; Perlich, J.; Diethert, A.; Wang, W.; Memesa, M.; Gutmann, J. S.; Majkova, E.; Capek, I. c.; Roth, S. V.; Petry, W.; Müller-Buschbaum, P. Array of Magnetic Nanoparticles via Particle Co-operated Self-Assembly in Block Copolymer Thin Film. *Macromolecules* **2009**, *42*, 6202−6208.

(35) Abul Kashem, M. M.; Perlich, J.; Schulz, L.; Roth, S.; Petry, W.; Müller-Buschbaum, P. Maghemite Nanoparticles on Supported Diblock Copolymer Nanostructures. *Macromolecules* **2007**, *40*, 5075−5083.

(36) Yao, Y.; Metwalli, E.; Niedermeier, M. A.; Opel, M.; Lin, C.; Ning, J.; Perlich, J.; Roth, S. V.; Müller-Buschbaum, P. Nano- and Microstructures of Magnetic Field-Guided Maghemite Nanoparticles in Diblock Copolymer Films. *ACS Appl. Mater. Interfaces* **2014**, *6*, 5244−5254.

(37) Schild, H. G. Poly(*N*-isopropylacrylamide): Experiment, Theory and Application. *Prog. Polym. Sci.* **1992**, *17*, 163−249.

(38) Tanaka, T. Collapse of Gels and the Critical Endpoint. *Phys. Rev. Lett.* **1978**, *40*, 820−823.

(39) Stuart, M. A. C.; Huck, W. T. S.; Genzer, J.; Müller, M.; Ober, C.; Stamm, M.; Sukhorukov, G. B.; Szleifer, I.; Tsukruk, V. V.; Urban, M.; Winnik, F.; Zauscher, S.; Luzinov, I.; Minko, S. Emerging Applications of Stimuli-Responsive Polymer Materials. *Nat. Mater.* **2010**, *9*, 101−113.

(40) Wang, W.; Kaune, G.; Perlich, J.; Papadakis, C. M.; Bivigou Koumba, A. M.; Laschewsky, A.; Schlage, K.; Röhlsberger, R.; Roth, S. V.; Cubitt, R.; Müller-Buschbaum, P. Swelling and Switching Kinetics of Gold Coated End-Capped Poly(*N*-isopropylacrylamide) Thin Films. *Macromolecules* **2010**, *43*, 2444−2452.

(41) Wang, W.; Troll, K.; Kaune, G.; Metwalli, E.; Ruderer, M.; Skrabania, K.; Laschewsky, A.; Roth, S. V.; Papadakis, C. M.; Müller-Buschbaum, P. Thin Films of Poly(*N*-isopropylacrylamide) End-Capped with *n*-Butyltrithiocarbonate. *Macromolecules* **2008**, *41*, 3209−3218.

(42) Adelsberger, J.; Kulkarni, A.; Jain, A.; Wang, W.; Bivigou-Koumba, A. M.; Busch, P.; Pipich, V.; Holderer, O.; Hellweg, T.; Laschewsky, A.; Müller-Buschbaum, P.; Papadakis, C. M. Thermoresponsive PS-*b*-PNIPAM-*b*-PS Micelles: Aggregation Behavior, Segmental Dynamics, and Thermal Response. *Macromolecules* **2010**, *43*, 2490−2501.

(43) Shenhar, R.; Norsten, T. B.; Rotello, V. M. Polymer-Mediated Nanoparticle Assembly: Structural Control and Applications. *Adv. Mater.* **2005**, *17*, 657−669.

(44) Shinjo, T.; Okuno, T.; Hassdorf, R.; Shigeto, K.; Ono, T. Magnetic Vortex Core Observation in Circular Dots of Permalloy. *Science* **2000**, *289*, 930−932.

(45) Cowburn, R. P.; Koltsov, D. K.; Adeyeye, A. O.; Welland, M. E.; Tricker, D. M. Single-Domain Circular Nanomagnets. *Phys. Rev. Lett.* **1999**, *83*, 1042−1045.

(46) Cowburn, R. Property Variation with Shape in Magnetic Nanoelements. *J. Phys. D: Appl. Phys.* **2000**, *33*, R1−R16.

(47) Skrabania, K.; Miasnikova, A.; Bivigou-Koumba, A. M.; Zehm, D.; Laschewsky, A. Examining the UV-vis Absorption of RAFT Chain Transfer Agents and Their Use for Polymer Analysis. *Polym. Chem.* **2011**, *2*, 2074−2083.

(48) Troll, K.; Kulkarni, A.; Wang, W.; Darko, C.; Bivigou Koumba, A. M.; Laschewsky, A.; Müller-Buschbaum, P.; Papadakis, C. M. The Collapse Transition of Poly(styrene-*b*-(N-isopropyl acrylamide)) Diblock Copolymers in Aqueous Solution and in Thin Films. *Colloid Polym. Sci.* **2008**, *286*, 1079−1092.

(49) Cabuil, V.; Hochart, N.; Perzynski, R.; Lutz, P. J. In *Trends in Colloid and Interface Science VIII*; Ottewill, R. H., Rennie, A. R., Eds.; Springer-Verlag: New York, 1994; Chapter 15, pp 71−74.

(50) Müller-Buschbaum, P. Influence of Surface Cleaning on Dewetting of Thin Polystyrene Films. *Eur. Phys. J. E* 2003, *12*, 443−448.

(51) Nečas, D.; Klapetek, P.; Gwyddion. An Open-Source Software for SPM Data Analysis. *Cent. Eur. J. Phys.* 2012, *10*, 181−188.

(52) Santoro, G.; Buffet, A.; Döhrmann, R.; Yu, S.; Körstgens, V.; Müller-Buschbaum, P.; Gedde, U.; Hedenqvist, M.; Roth, S. V. Use of Intermediate Focus for Grazing Incidence Small and Wide Angle X-Ray Scattering Experiments at the Beamline P03 of Petra III, DESY. *Rev. Sci. Instrum.* 2014, *85*, 043901.

(53) Buffet, A.; Rothkirch, A.; Dohrmann, R.; Körstgens, V.; Abul Kashem, M. M.; Perlich, J.; Herzog, G.; Schwartzkopf, M.; Gehrke, R.; Müller-Buschbaum, P. P03, the Microfocus and Nanofocus X-Ray Scattering (MiNaXS) Beamline of the Petra III Storage Ring: The Microfocus Endstation. *J. Synchrotron Radiat.* 2012, *19*, 647−653.

(54) Müller-Buschbaum, P. Grazing Incidence Small-Angle X-Ray Scattering: An Advanced Scattering Technique for the Investigation of Nanostructured Polymer Films. *Anal. Bioanal. Chem.* 2003, *376*, 3−10.

(55) Knoll, A.; Horvat, A.; Lyakhova, K.; Krausch, G.; Sevink, G.; Zvelindovsky, A.; Magerle, R. Phase Behavior in Thin Films of Cylinder-Forming Block Copolymers. *Phys. Rev. Lett.* 2002, *89*, 035501.

(56) Coulon, G.; Russell, T. P.; Deline, V. R.; Green, P. F. Surface-Induced Orientation of Symmetric, Diblock Copolymers: A Secondary Ion Mass-Spectrometry Study. *Macromolecules* 1989, *22*, 2581−2589.

(57) Lopes, W. A.; Jaeger, H. M. Hierarchical Self-Assembly of Metal Nanostructures on Diblock Copolymer Scaffolds. *Nature* 2001, *414*, 735−738.

(58) Ramanathan, M.; Nettleton, E.; Darling, S. B. Simple Orientational Control over Cylindrical Organic−Inorganic Block Copolymer Domains for Etch Mask Applications. *Thin Solid Films* 2009, *517*, 4474−4478.

(59) Kampmann, R.; Haese-Seiller, M.; Kudryashov, V.; Nickel, B.; Daniel, C.; Fenzl, W.; Schreyer, A.; Sackmann, E.; Rädler, J. Horizontal ToF-Neutron Reflectometer REFSANS at FRM-II Munich/Germany: First Tests and Status. *Phys. B* 2006, *385*, 1161−1163.

(60) Kim, S. O.; Solak, H. H.; Stoykovich, M. P.; Ferrier, N. J.; de Pablo, J. J.; Nealey, P. F. Epitaxial Self-Assembly of Block Copolymers on Lithographically Defined Nanopatterned Substrates. *Nature* 2003, *424*, 411−414.

(61) Kellogg, G. J.; Walton, D. G.; Mayes, A. M.; Lambooy, P.; Russell, T. P.; Gallagher, P. D.; Satija, S. K. Observed Surface Energy Effects in Confined Diblock Copolymers. *Phys. Rev. Lett.* 1996, *76*, 2503−2506.

(62) Reddy, B. *Advances in Diverse Industrial Applications of Nanocomposites*, 1st ed; InTech: Rijeka, 2011.

(63) Chiu, J. J.; Kim, B. J.; Kramer, E. J.; Pine, D. J. Control of Nanoparticle Location in Block Copolymers. *J. Am. Chem. Soc.* 2005, *127*, 5036−5037.

(64) Huh, J.; Ginzburg, V. V.; Balazs, A. C. Thermodynamic Behavior of Particle/Diblock Copolymer Mixtures: Simulation and Theory. *Macromolecules* 2000, *33*, 8085−8096.

(65) Yeh, S.-W.; Wei, K.-H.; Sun, Y.-S.; Jeng, U.-S.; Liang, K. S. Cds Nanoparticles Induce a Morphological Transformation of Poly (styrene-*b*-4-vinylpyridine) from Hexagonally Packed Cylinders to a Lamellar Structure. *Macromolecules* 2005, *38*, 6559−6565.

(66) Ojeda-Lopez, M. A.; Needleman, D. J.; Song, C.; Ginsburg, A.; Kohl, P. A.; Li, Y.; Miller, H. P.; Wilson, L.; Raviv, U.; Choi, M. C.; Safinya, C. R. Transformation of Taxol-Stabilized Microtubules into Inverted Tubulin Tubules Triggered by a Tubulin Conformation Switch. *Nat. Mater.* 2014, *13*, 195−203.

(67) Tsori, Y.; Sivaniah, E.; Andelman, D.; Hashimoto, T. Orientational Transitions in Symmetric Diblock Copolymers on Rough Surfaces. *Macromolecules* 2005, *38*, 7193−7196.

(68) Kaune, G.; Ruderer, M. A.; Metwalli, E.; Wang, W.; Couet, S.; Schlage, K.; Röhlsberger, R.; Roth, S. V.; Müller-Buschbaum, P. In Situ

GISAXS Study of Gold Film Growth on Conducting Polymer Films. *ACS Appl. Mater. Interfaces* 2008, *1*, 353−360.

(69) Abul Kashem, M. M.; Perlich, J.; Schulz, L.; Roth, S. V.; Müller-Buschbaum, P. Correlated Roughness in Polymer Films Containing Maghemite Nanoparticles. *Macromolecules* 2008, *41*, 2186−2194.

(70) Babonneau, D.; Camelio, S.; Lantiat, D.; Simonot, L.; Michel, A. Waveguiding and Correlated Roughness Effects in Layered Nanocomposite Thin Films Studied by Grazing-Incidence Small-Angle X-Ray Scattering. *Phys. Rev. B* 2009, *80*, 155446.

(71) Müller-Buschbaum, P.; Gutmann, J. S.; Lorenz, C.; Schmitt, T.; Stamm, M. Decay of Interface Correlation in Thin Polymer Films. *Macromolecules* 1998, *31*, 9265−9272.

(72) González, D. M.; Körstgens, V.; Yao, Y.; Song, L.; Santoro, G.; Roth, S. V.; Müller-Buschbaum, P. Improved Power Conversion Efficiency of P3HT:PCBM Organic Solar Cells by Strong Spin−Orbit Coupling-Induced Delayed Fluorescence. *Adv. Energy Mater.* 2015, *5*, 1401770(1.

(73) Fasolka, M. J.; Banerjee, P.; Mayes, A. M.; Pickett, G.; Balazs, A. C. Morphology of Ultrathin Supported Diblock Copolymer Films: Theory and Experiment. *Macromolecules* 2000, *33*, 5702−5712.

(74) Schulz, L.; Schirmacher, W.; Omran, A.; Shah, V.; Böni, P.; Petry, W.; Müller-Buschbaum, P. Elastic Torsion Effects in Magnetic Nanoparticle Diblock-Copolymer Structures. *J. Phys.: Condens. Matter* 2010, *22*, 346008.

(75) Xia, X.; Metwalli, E.; Ruderer, M. A.; Körstgens, V.; Busch, P.; Böni, P.; Müller-Buschbaum, P. Nanostructured Diblock Copolymer Films with Embedded Magnetic Nanoparticles. *J. Phys.: Condens. Matter* 2011, *23*, 254203.

(76) Blundell, S. *Magnetism in Condensed Matter*, 1st ed; Oxford University Press: New York, 2001.

(77) Néel, L. Théorie Du Traînage Magnétique Des Ferromagnétiques en Grains Fins avec Applications aux Terres Cuites. *Ann. Géophys* 1949, *5*, 99−136.

(78) Brown, W. F. J. Thermal Fluctuations of a Single-Domain Particle. *Phys. Rev.* 1963, *130*, 1677.

(79) Bean, C. P.; Jacobs, I. S. Magnetic Granulometry and Super-Paramagnetism. *J. Appl. Phys.* 1956, *27*, 1448−1452.